Particle-Size Effect in Airborne Standing-Wave Acoustic Levitation: Trapping Particles at Pressure Antinodes

Jhon F. Pazos Ospina,[1] Victor Contreras,[2] Jordan Estrada-Morales,[3] Diego Baresch,[4] Joao Luis Ealo,[1,5] and Karen Volke-Sepúlveda[3,*]

[1] *School of Mechanical Engineering, Universidad del Valle, Cali 760032, Colombia*
[2] *Instituto de Ciencias Físicas, Universidad Nacional Autónoma de México, Cuernavaca Morelos 62210, Mexico*
[3] *Instituto de Física, Universidad Nacional Autónoma de México, Cd. de México, C.P. 04510, Mexico*
[4] *Université de Bordeaux, CNRS, Bordeaux INP, ENSAM, INRAE, UMR 5295 I2M, Talence F-33405, France*
[5] *Centro de Investigación e Innovación en Bioinformática y Fotónica-CiBioFi, Universidad del Valle, Cali 760032, Colombia*

(Received 13 February 2022; revised 14 May 2022; accepted 17 June 2022; published 12 September 2022)

It is well known that a particle put into an ultrasonic standing wave tends to move towards an equilibrium position, where the acoustic pressure-induced force on its surface compensates the particle weight. We demonstrate, by means of a full three-dimensional numerical analysis and a thorough experimental study, that the acoustic force, and thus the particle's behavior, critically depends on its size. While particles within certain size ranges, including those smaller than half the wavelength, are trapped on axis around the pressure nodes, particles in other size ranges are trapped off axis nearby the pressure antinodes. This behavior, related with sign inversions of the radiation force, implies that the magnitude of the force, and thus the trapping stiffness, can be maximum or null for some specific sizes. As a case of study, we analyze expanded polystyrene particles levitated in air with an ultrasonic frequency of 40 kHz, a relevant system due to recent applications for the development of volumetric displays. Yet, our results illustrate a general behavior of radiation-based traps with structured wave fields.

DOI: 10.1103/PhysRevApplied.18.034026

I. INTRODUCTION

The idea of using acoustic waves for positioning matter by virtue of hydrodynamical forces dates back to the 19th century, with the experimental work by Kundt with standing sound waves in a resonant tube [1]. A little after, Lord Rayleigh set the basis for the study of scattering of sound waves by small balls in Volume II of his famous "Theory of sound" [2], which in turn would provide solid theoretical grounds for King's study on the acoustic radiation force in 1934 [3]. However, it has been Gor'kov's approach for the calculation of this force on an object much smaller than the wavelength in an ideal fluid, which has prevailed overtime due to its elegance and simplicity [4], but also because of its great success in predicting experimental observations [5]. According to Gor'kov, the potential of the conservative acoustic force is proportional to the mean-square fluctuations of the pressure and particle velocity of the wave at the point where the particle is located [4]. In air, the result is that small particles are attracted towards the regions with the lowest time-averaged acoustic pressure and the highest particle velocity [6,7]. In a standing wave, these two conditions are simultaneously satisfied at the pressure nodes. This is why the earliest acoustic levitation devices were designed using single-axis standing-wave configurations, with the aim of positioning matter in space first and then in terrestrial laboratories [8–10].

As ultrasonic transducers and the design of resonant cavities have improved, the technique of acoustic levitation in midair has risen as a major tool for containerless analysis and processing of materials [11–19]. For example, by using a high-power Langevin transducer and a concave reflector with appropriate geometrical parameters [20], the magnitude of the acoustic forces can be enhanced to levitate the heaviest solids and liquids in air [21]. Also, by controlling the standing acoustic wave in space and time, samples can be brought in contact to initiate chemical reactions [22] or the agglomeration and growth of ice particles can be achieved [23].

*karen@fisica.unam.mx

Experimentally, acoustic trapping and levitation has undergone a renaissance over the last decade, due to a different technical approach: the high-power transducer was replaced by phased arrays of low-power ultrasonic emitters, whose main advantage is to allow the dynamic reconfiguration of the acoustic field [5,22,24]. This concept expanded the capabilities of acoustic traps, making it possible to control the motion of objects along one or two dimensions by using either a single phased array and a reflector [22] or pairs of confronted phased arrays along orthogonal axes [24,25]. Phased arrays also led to the development of dynamic acoustic holography, which increased the manipulation volume and avoided the multiple-axes configurations [26,27]. Indeed, holographic elements produced by electronically controlling the phase of each emitter have allowed rotation and translation of particles along complex three-dimensional (3D) trajectories using a single-sided array. Of note, all these airborne manipulation techniques rely on the appropriate structuring of the acoustic field to generate pressure nodes in 3D, where the particles can be trapped.

Despite the widespread use of standing waves for levitation, little is still known on the levitation stability when the particle size is comparable to, or larger than, the driving wavelength. One possible reason for this gap is that the modeling of the radiation force is not straightforward. Gor'kov's acoustic potential approach is valid for particle sizes roughly below $D/\lambda \sim 0.1$, where D is the particle diameter and λ the wavelength, and this limit may depend on the physical properties of the particle (density and compressibility). On this scale, fluctuations of the pressure field and of its first-order gradient (velocity field) are sufficient to describe the forced dynamics of the particle and higher-order spatial fluctuations can be safely ignored. However, size effects for larger particles are expected, including shape oscillations and conditions of resonance, which should greatly modify the dynamics of a levitated particle. Another possible reason is that, experimentally, the generation of a resonant standing wave in the presence of a large scattering particle is not always feasible. Indeed, in the common single-axis configuration comprising a source and a perfect reflector, the presence of the particle obstructs the emitted field that would otherwise reach the reflector, making it hard to attain a resonance of the cavity. Understanding this regime is useful to trap larger objects with acoustic waves and could enable precise measurements of mechanical properties of the levitated objects [28].

In fact, considerable efforts have been invested in exploring the upper limits of the size of the objects that can be trapped or manipulated in air with acoustic waves. For example, near-field strategies for levitation at a height h, much smaller than the wavelength λ, have been implemented to hold and move large and heavy objects with a planar geometry by using the flexural waves excited along a vibrating plate [29]. Another approach for short-distance levitation has been to generate standing waves between the sound radiator and the object, implemented so far in planar geometry as well [30] and for a big sphere suspended by a tripodlike arrange of transducers [31]. Regarding schemes relying on phased arrays, a technique based on the generation of sequences of short-pulsed acoustic vortices with helicity of equal magnitude but opposite chirality was introduced in 2018, such that the angular-momentum transfer can be tuned while a particle of the order of the wavelength can be trapped in three dimensions at the central pressure node of the focused time-averaged vortex. As the size of the node increases with the topological charge, so does the maximum size of the particles that can be stably trapped at distances of several wavelengths from the transducers [32]. More recently, a numerical design technique, named "boundary hologram method," was implemented [33]. In this case, the drive of the phased array is numerically optimized to yield a static levitation field that stabilizes the body's position and rotation for macroscopic nonspherical rigid bodies larger than the sound wavelength. Again, this method yields a low-pressure trapping volume, circumvented by high acoustic intensity regions, and adapted to the geometry of the object. Nevertheless, the field optimization approach is not able to adapt to changes in particle size or material properties, which calls for a better understanding of the trapping dynamics of large objects in levitation fields.

In this work, we present a full three-dimensional analysis of the acoustic radiation forces exerted on particles with size comparable to the wavelength in a standing-wave levitation device in air. For this purpose, we use the theoretical model developed in Ref. [34], based on the generalized Lorenz-Mie theory (GLMT), well established in optics. Our results show that for this size regime, the force exhibits sign inversions as a function of particle size, which implies that some particles will stably levitate at the highest average-pressure regions of a standing wave, in clear contrast with previous work establishing the stable equilibrium position of smaller particles near acoustic pressure nodes. Detecting this variation of the force is only possible by using a model valid beyond the size range in which the force is obtained as the gradient of an acoustic potential [4]. We also show that there is an optimum particle size for which the acoustical trapping force is maximum for a given frequency. Regarding the transverse forces in the case of a focused single-axis levitator, we reveal that particles levitating at the pressure antinodes find a transverse equilibrium off axis. We experimentally demonstrate our numerical observations and, moreover, we directly visualize the acoustic waves and the particle's relative position with respect to the pressure field by using schlieren imaging [35].

II. STANDING-WAVE ACOUSTIC LEVITATION BEYOND THE SMALL-PARTICLE APPROXIMATION

The generalized Lorenz-Mie theory for the calculation of radiation forces, which is valid regardless of the particle size, position, and topology of the incident wave front, was introduced in optics in 1988 [36] and recently successfully developed in acoustics [34,37–39]. The theoretical framework described in Ref. [34] has been experimentally validated in the context of the acoustic manipulation of solid particles and bubbles in liquids using single-beam acoustic traps [40,41]. The analysis is based on the scattering of an arbitrary acoustic field by an elastic spherical particle, which is allowed to be arbitrarily located in an inviscid fluid.

In brief, following the procedure described in detail in Ref. [34], the monochromatic incident field is expanded in a set of spherical harmonics in the basis centered on the particle (r,θ,φ):

$$\phi_i = \phi_0 e^{-i\omega t} \sum_{n=0}^{\infty} \sum_{m=-n}^{n} A_n^m j_n(kr) Y_n^m(\theta,\varphi), \qquad (1)$$

where ϕ_i is the complex acoustic velocity potential related to the complex acoustic pressure change as $p = -\rho_m \partial\phi/\partial t$, with ρ_m being the external medium density, $\omega = 2\pi f$ the angular frequency, f the frequency, $k = \omega/c$ the wave number, and c the speed of sound in the medium. j_n represent the spherical Bessel functions of the first kind and $Y_n^m = P_n^m(\cos\theta)e^{im\varphi}$ are complex spherical harmonics formed with the associated Legendre functions, P_n^m. To describe the incident ultrasonic standing field generated by two counterpropagating beams, either plane or focused wave fronts, the beam-shape coefficients A_n^m in Eq. (1) are obtained as the superposition of a subset of two fields, $A_n^m = a_n^m + \tilde{a}_n^m$. The first set of coefficients is obtained using spherical functions that involve the acoustic frequency, the transducer's radius of curvature (in the case of focused beams) and aperture size [38]. The second set $\tilde{a}_n^m$ describes the counterpropagating beam and can be obtained by applying rotation relations for spherical harmonics to a_n^m, using a rotation matrix with angle π about the y axis [34]. By using the semianalytical formulation of Ref. [38], we suppose each beam is generated by a concave and baffled aperture, and freely propagates in a semi-infinite free space. Therefore, we neglect the reflections that arise when each beam interacts with the opposite surface. The good agreement between the experimental and modeled fields presented later in this work confirm this is a reasonable assumption in our configuration.

The interaction of the incident field with the trapped particle is obtained by computing the scattered field in the same spherical basis:

$$\phi_s = \phi_0 e^{-i\omega t} \sum_{n=0}^{\infty} \sum_{m=-n}^{n} R_n A_n^m h_n^{(1)}(kr) Y_n^m(\theta,\varphi), \qquad (2)$$

where $h_n^{(1)}$ is the spherical Hankel function of the first kind and the expression of the scattering coefficients, R_n, are well established for elastic particles, and depend on the mechanical properties of the particle and the surrounding fluid (see, e.g., Refs. [34,37]). The initial beam-shape coefficients, A_n^m, describe the configuration where the sphere is located on axis at the coincident center of curvature of both concave surfaces [34,38]. The position of the particle relative to this position in the incident field (x,y,z) can be changed by applying rotation and translation relations to these coefficients. Following Ref. [34], the radiation force components acting on the center of the particle, F_x, F_y, and F_z, are computed from the total acoustic field [sum of Eqs. (1) and (2)] and are functions of the vertical position z of the particle and its transverse position, (x,y). The force components involve infinite series (truncated numerically) of the beam shape and scattering coefficients. Noteworthy, the first two terms of these series, $n = 0$ and $n = 1$, corresponding to the monopolar and dipolar contribution to the acoustic force, reduce to Gor'kov's popular expression of the so-called gradient force in the limit of small particles relative to the wavelength [4,40].

Here we analyze the acoustic force per Pa^2, $f_z = F_z\ \mathrm{Pa}^{-2}$, and $f_x = F_x\ \mathrm{Pa}^{-2}$, exerted on an expanded polystyrene (EPS) particle (of density $\rho_p = 13.8\ \mathrm{kg\ m}^{-3}$) in air ($\rho_m = 1.2\ \mathrm{kg\ m}^{-3}$) by an ultrasound field with a frequency of 40 kHz. Compression and transverse acoustic wave velocity in the particle are $c_l = 900\ \mathrm{m\ s}^{-1}$ and $c_t = 700\ \mathrm{m\ s}^{-1}$, respectively, while $c = 343\ \mathrm{m\ s}^{-1}$ is the speed of sound in air.

First, we consider the ideal case of a plane standing wave, where no transverse forces are expected. Figure 1(a) presents a comparison of the maximum axial force f_z, calculated at a fixed z plane ($z = 0.125\lambda$), using Gor'kov's approximation (black dotted line) and the GLMT (red dashed line) as a function of the parameter D/λ, with D being the particle diameter and λ the wavelength of the acoustic field. It is seen from the close up in the inset that both calculations coincide well for $D <\sim 0.15\lambda$. However, according to Gor'kov's approximation, the maximum force keeps growing as the particle size increases, while the GLMT gives rise to an optimum value of the force for $D \simeq 0.4\lambda$, then the force decreases and becomes null for $D \simeq 0.6\lambda$ before a sign inversion. This is of note, since the magnitude of the force is related with the trapping stiffness.

In order to interpret the sign inversions of the force, a full force map is presented in Fig. 1(b) as a function of D/λ and the position z/λ along the levitator axis. As a reference, the pressure-field amplitude is illustrated on the right.

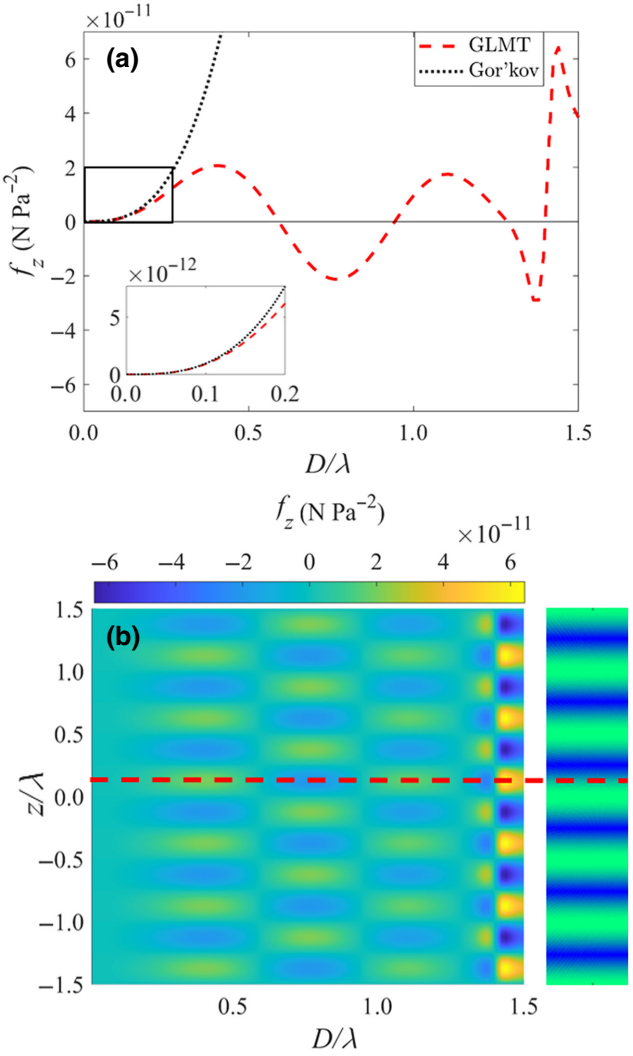

FIG. 1. Acoustic radiation force in a plane standing wave. (a) Axial radiation force per Pa^2, f_z, exerted by a plane standing acoustic wave on an EPS spherical particle of diameter D suspended in air as a function of the parameter D/λ; the particle is located at $z = 0.125\lambda$, considering that $z = 0$ corresponds to a pressure antinode. The black dotted line represents Gor'kov's approximation, while the red dashed line shows the results for the GLMT. Inset: close up of the square-enclosed region. (b) Map of f_z as a function of particle size (D/λ) and position z/λ. The red dashed line corresponds to the plot in (a). On the right, the absolute value of the normalized pressure field is illustrated as a reference; the dark (blue) color corresponds to the nodes.

The horizontal red dashed line corresponds to the cross section plotted in Fig. 1(a). The map shows a set of vertical bands through which the axial force is quasiperiodic, alternating between positive (bright) and negative (dark) values for a given particle size. Each band corresponds to a different behavior regime, where the force distribution is out of phase with respect to its neighbors. Stable equilibrium points along the z axis for a given value of D/λ occur at the zero crossings from a positive to a negative region. Therefore, while particles with $D <\sim 0.6\lambda$ and $\sim 0.95 < D/\lambda <\sim 1.25$ find stable equilibrium positions at the pressure nodes, particles with $\sim 0.6 < D/\lambda <\sim 0.95$ experience stable equilibrium at the pressure antinodes. This contrasting behavior was investigated in two previous one-dimensional theoretical studies, one for solid particles in liquid [42] and the other for two liquid particles in air whose sizes differ in one order of magnitude [39]. This effect has several unnoticed implications. Observe, for instance, that the particles whose size lies in between the bands cannot be trapped in a standing plane wave, since the force vanishes everywhere along the z axis. The sign inversions and the vanishing force can be attributed to the contribution of the higher-order multipoles to the total change in the momentum flux, caused by the interaction between the particle and the acoustic field. Indeed, the higher multipole terms become relevant for large particles, and seem to give rise to equal contributions to the radiation stresses applied on the upper and lower surfaces of the sphere [43]. Finally, we also observe that particles with $D >\sim 1.25\lambda$ exhibit a different behavior, where the force magnitude grows abruptly before and after a sign inversion around specific values of D/λ, which correspond to mechanical resonances of the particle [44,45]. Hereafter, we use the term *size effect* to refer to the magnitude and sign dependence of the acoustic radiation force on the size of the particle.

It is worthwhile to remark that the radiation force map in terms of (D/λ, z/λ) for a plane standing wave is identical regardless of the specific frequency of the acoustic field, which means that we can always find optimum particle sizes to maximize the acoustic force magnitude at a given frequency and vice versa. For example, the first optimum value of the force (maximum trapping stiffness) for levitation nearby the nodes is achieved when $D \sim 0.40\lambda$, which corresponds to diameters of 3.4 and 4.9 mm for frequencies of 40 and 28 kHz, respectively. As the magnitude of the radiation force scales with the acoustic energy density [34], the vibration amplitude of the transducers could always be adjusted (in principle, not necessarily in practice) to counteract the weight of a given particle. However, Fig. 1 suggests that considerably lower pressure levels would be required for levitating a particle whose size corresponds to an optimum magnitude of the force [maxima and minimum at Fig. 1(a)]. This result might be of considerable practical interest for the development of 3D display technology using EPS spheres in air [25,46]. Yet, a full dynamical analysis, taking into account the weight and viscous drag, would be required to determine optimum trapping conditions for a particle that is rapidly moving in air, as well as additional mechanical effects due to the fast acoustic field reconfiguration.

Now we consider a focused single-axis standing-wave acoustic levitator in a symmetric concentric configuration

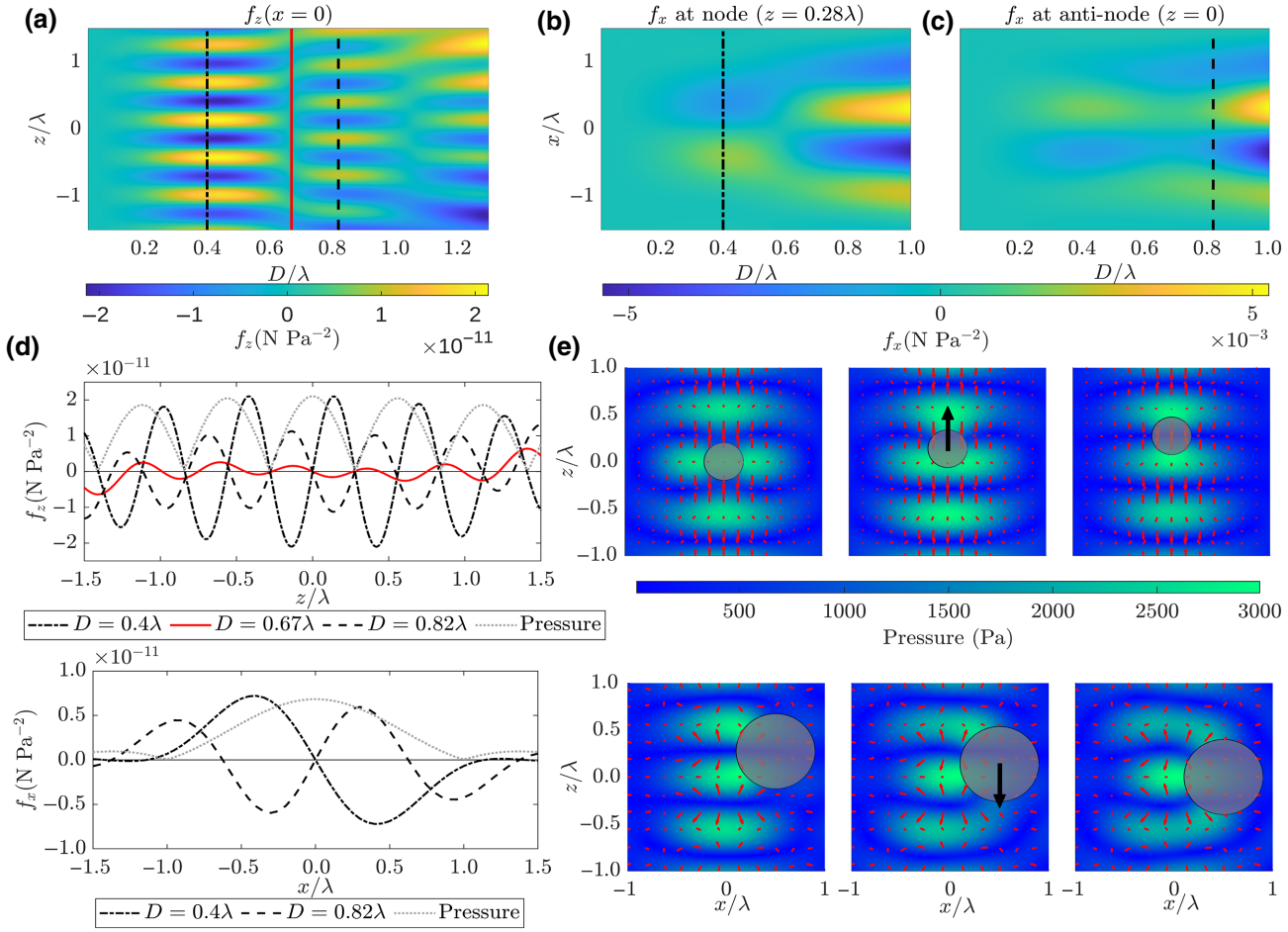

FIG. 2. Acoustic forces acting upon a particle within a single-axis symmetric concentric levitator. (a) z component of the force per Pa^2, f_z, as a function of particle size (D/λ) and position z/λ, when $(x, y) = (0, 0)$ (on axis). (b),(c) show the x component of the transverse force f_x vs D/λ and x/λ, calculated at the transverse planes $z = 0.28\lambda$ (pressure node of the focused field) and $z = 0$ (pressure antinode), respectively. (d) Top: axial force f_z as a function of z/λ for particles of different sizes located on axis. (d) Bottom: f_x vs x/λ for particles of sizes $D = 0.40\lambda$ located at the pressure node ($z = 0.28\lambda$) and $D = 0.82\lambda$ located at the pressure antinode ($z = 0$). Gray line in both plots represents the acoustic pressure magnitude as a reference. (e) In the background, pressure amplitude and radiation force field (red arrows) for particles with diameters of 0.40λ (top row) and 0.82λ (bottom row) at the plane $y = 0$. In the left column, both particles are illustrated in unstable equilibrium positions. In the central column, black arrows indicate the direction of the net force acting on each particle at this location (not in scale). In the right column, particles have reached stable equilibrium positions.

based on the TinyLev design [27], i.e., with an upper and lower concave spherical caps with equal radii of curvature R_c separated by a distance $L \sim 2R_c$, which corresponds to our experimental device. The curvature of the sources plays a role in the particle positioning. Pressure gradients due to the focusing of the field make the particle experience forces in the transverse direction (x-y plane), but also modify the axial force, as can be appreciated from Fig. 2(a), showing f_z vs (D/λ, z/λ). In comparison with Fig. 1(b), the magnitude of the force lowers in the second vertical band, whereas the third band is more affected by the pressure gradient and wave-front curvature arising from the focusing of the field. Namely, for particles with $D >\sim \lambda$ there is an increase of the axial force magnitude outward from $z = 0$, being positive for $z > 0$ and negative for $z < 0$. This is presumably due to the envelope pressure gradient having a maximum at the focal point at $z = 0$; the larger the particle, the more sensitive it becomes to the effect of this long-range gradient. In contrast, small particles respond basically to short-range gradients due to the standing wave and are not sensitive to the wave-front curvature.

The axial force along z/λ for different particle sizes can be better appreciated from the top plot of Fig. 2(d), showing f_z along the vertical lines represented in (a), where stable equilibrium points correspond to zero crossings with

negative slope. The profile of the acoustic pressure amplitude is also illustrated (gray dotted line) as a reference. Clearly, the smaller particle ($D = 0.4\lambda$, dash-dotted curve) has stable equilibrium points at the pressure nodes, while the larger particle ($D = 0.82\lambda$, dashed curve) has stable equilibrium at the pressure antinodes. Here we can also see that, in comparison, the force is very weak for a particle with diameter $D = 0.67\lambda$ (red solid curve), although not null, due to the wave-front curvature.

To determine whether a particle can indeed be trapped or not, it is necessary to simultaneously analyze the transverse acoustic force at the z planes where it exhibits axial stable equilibrium. Namely, the x component of the force per Pa^2, f_x, as a function of D/λ and the transverse position x/λ is presented in Figs. 2(b) and 2(c) at the planes $z = 0.28\lambda$ (pressure node for the focused field) and $z = 0$ (pressure antinode), respectively. From Fig. 2(b) we can see that a particle with $D = 0.4\lambda$ has a stable equilibrium point at $x = 0$, hence it can be trapped on axis at the pressure node. The same behavior is expected to occur at the neighbor nodes, upwards and downwards. On the other hand, Fig. 2(c) indicates that the particle with $D = 0.82\lambda$ does not exhibit stable equilibrium on axis, but at $x \approx \pm 0.52\lambda$, where the transition from a bright to a dark region in the force map is located. This is more clearly appreciated at the bottom plot of Fig. 2(d), showing the normalized transverse force for the two particle sizes illustrated in the vertical lines of Figs. 2(b) and 2(c) at the pressure node and antinode, respectively. Noteworthy, the system has rotational symmetry around the z axis, which means that the off-axis equilibrium points for the larger particle correspond to a circumference of radius $\rho = \sqrt{x^2 + y^2} \approx 0.52\lambda$, where the particle is free to move around in the angular direction (see Fig. 3). As the particle size increases, its surface becomes sensitive to the curvature of the impinging wave fronts. Therefore, there seems to be a curvature-driven unbalance of the radiation stress acting on the surface of the sphere, which results in the off-axis equilibrium.

Recapping, while small particles can be levitated on axis near the pressure nodes, larger particles would be trapped *off axis* near the *pressure antinodes*. This is graphically summarized in Fig. 2(e): the left column shows an unstable equilibrium position for both particles, in the central column the black arrow illustrates the net force direction (not in scale) and motion trend when the particle is located midway between the node and the antinode, and the right column shows the stable trapping position for both particles. The total pressure field (incident + scattered) and the vector force field (red arrows) are included in the background. The vector field represents the net force acting on a particle whose center is located at the position of each arrow onset. The standing-wave distribution may be significantly modified by the scattered field, depending on the particle size and position, as it is apparent in the bottom-right image of Fig. 2(e). This also impacts the distribution of the radiation stress on the surface of the sphere.

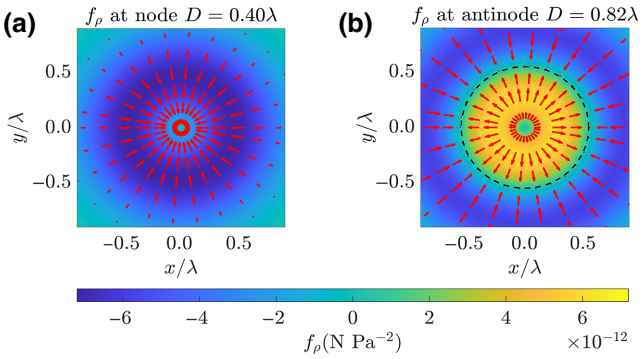

FIG. 3. Radial component of the acoustic radiation force, f_ρ, in the transverse plane for (a) the particle of $D = 0.40\lambda$ located at $z = 0.28\lambda$ and (b) the particle of $D = 0.82\lambda$ at $z = 0$. Red arrows indicate the vector force field acting on the particle at each position. Stable equilibrium is achieved where the arrows converge; the center in (a) and the dotted black circle in (b).

III. SIZE EFFECT: EXPERIMENTAL OBSERVATION

A. Experimental setup

In order to verify our theoretical results, we conduct a series of experiments using a single-axis symmetric concentric levitator [see Fig. 4(a)]. It consists of two concave spherical caps made of aluminum, with a radius of curvature of 60 mm, each one holding an array of 36 individual emitters (MSO-A1040H07T, Manorshi) distributed around in three concentric rings formed by 6, 12, and 18 transducers. The resultant radiating surface has a radius of curvature of 55 mm [35]. The operation frequency is 40 kHz in air and either a square or a sinusoidal continuous excitation signal is applied. The emitters are selected to have similar sensitivity and phase [27].

For demonstrating the size effect, we use spherical EPS particles with diameters in the range 1 mm $< D <$ 8 mm ($0.12\lambda - 0.95\lambda$). As the density of the EPS may vary over a wide range, we determine it from the direct measurement of the weight and diameter of the particle, giving $\rho_p = (13.8 \pm 0.33)$ kg m^{-3}. To observe and quantify the location of the levitated spheres within the ultrasonic standing wave, the pressure field is simultaneously characterized with two different methods. On the one hand, the acoustic pressure distribution is directly measured by using a calibrated microphone and a linear translation stage. On the other hand, a schlieren imaging system [47] is used to directly observe the acoustic waves and the relative position of the particles within the field.

Although, in principle, the distance between the two spherical caps in a concentric levitator would be $L = 2R_c$,

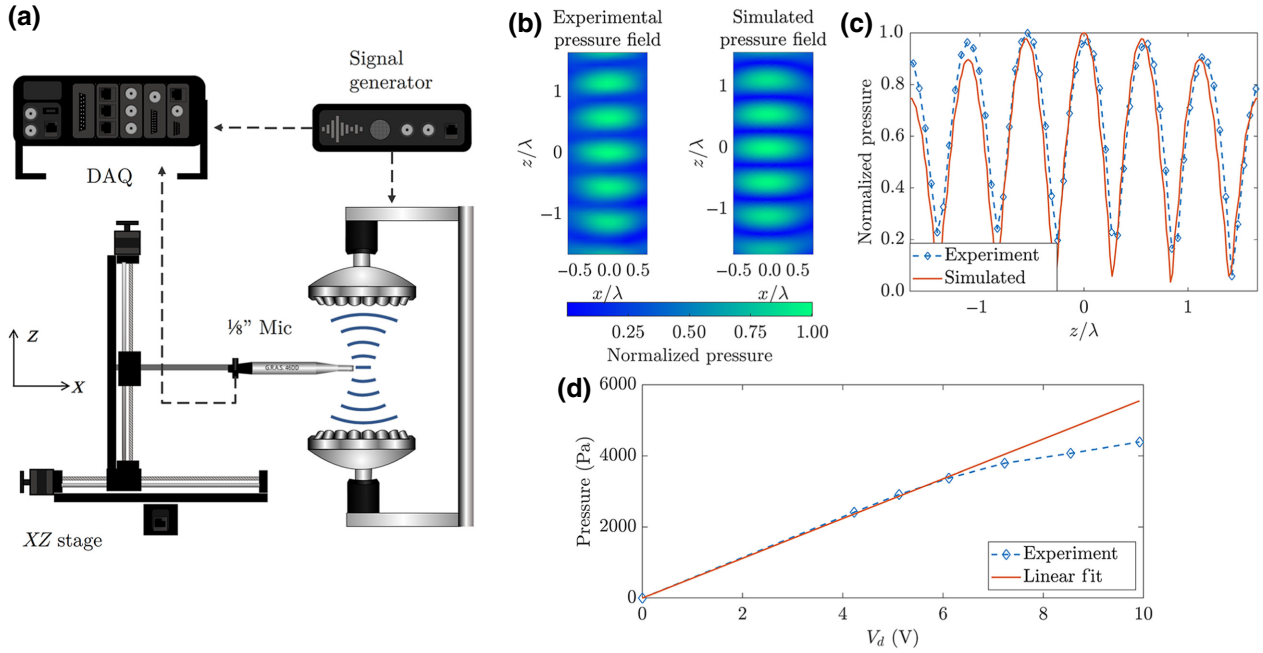

FIG. 4. Characterization of the acoustic pressure field. (a) Experimental setup for the generation and characterization of the standing wave, consisting of a symmetric concentric levitator, a 1/8" calibrated microphone attached to an *XZ* translation stage, an arbitrary signal generator and a data-acquisition system (DAQ). (b) Comparison between the experimentally measured and the simulated pressure-field distribution. (c) Experimental and simulated profiles of the normalized pressure along the acoustic axis. (d) Experimental measurement of the levitator sensitivity (maximum pressure amplitude P_0 against driving voltage V_d).

in practice it is necessary to adjust it to match a longitudinal mode of the cavity, so that the largest pressure gradients are achieved and the acoustic radiation forces optimized. For this purpose, one of the spherical surfaces is attached to a linear micrometric translation stage oriented along the *Z* axis. The cavity length is fixed to a distance where the contrast of the standing wave in the schlieren images is maximized while the electric current consumption is minimized, as reported elsewhere [35]. With this adjustment procedure, we set $L = 115$ mm along the main axis. In addition, small tilt deviations between the spherical caps are corrected by coupling one of them to a mechanical gimbal mount, whereas the other is attached to an *XY* translation stage to correct lateral misalignments. Of note, optimum alignment of the cavity and adjustment of its length are crucial to achieve the levitation of the larger spheres at the antinodes.

The acoustic pressure amplitude is characterized by using a calibrated microphone (1/8 inch, type 4138 Brüel & Kjær) attached to an *XZ* translation unit, as illustrated in Fig. 4(a). The microphone calibration is validated using a sound pistonphone (type 4231 Brüel & Kjær). A comparison between the experimentally measured (normalized) acoustic pressure and the corresponding simulation is presented in Figs. 4(b) and 4(c), showing a very good agreement. The field exhibits a homogeneous and symmetrical distribution around the center of the working volume.

To measure the pressure field within the levitator, the microphone is oriented perpendicularly to the field (90° incidence), thus it is necessary to experimentally determine a correction factor for the microphone sensitivity. To achieve this goal, we first measure the acoustic pressure for a single transducer, placing the microphone at a given distance in a collinear configuration (0° incidence). Then we repeat the measurements by reorienting the microphone in a 90°-incidence configuration, under otherwise equal conditions. A correction factor of 0.53 at 40 kHz is determined by comparing both measurements.

After the calibration procedure, we determine the levitator sensitivity, i.e., the maximum acoustic pressure as a function of the driving voltage $P_0(V_d)$. For this purpose, we place the microphone tip at the absolute maximum of the pressure field P_0 within the levitator, found with an *XZ* translation stage, and proceed to vary the operation voltage V_d. The results for the acoustic pressure against the driving voltage are calculated from the spectral analysis of the excitation and response signals at 40 kHz, in consistency with the theoretical calculations of the radiation force. We find that the data for $P_0(V_d)$ at 40 kHz starts departing from a linear behavior as V_d increases [see Fig. 4(d)]. This is mainly attributed to the unwanted excitation of higher harmonic frequencies (harmonic distortion) in the input signal. Further research is required for the study of the levitator performance at high-pressure operation. The values

of the pressure at arbitrary driving voltages are obtained by simple interpolation from the experimental data in Fig. 4(d). It is worth mentioning that reflections from the spherical caps can become non-negligible. This explains the relevance of optimizing the cavity length, so as the multiple reflections increase only the effective value of $P_0(V_d)$, without a significant spatial distortion of the field.

Schlieren system. We use a single-mirror schlieren configuration [47] to visualize the acoustic waves. It consists of a pointlike light source, a spherical mirror with a focal length $f = 1.5$ m, a commercial razor blade, and a digital single-lens reflex camera (6D, Canon) coupled to a telephoto lens (EF 100–400 mm, Canon). The spherical mirror is placed behind the levitating assembly, at a distance $2f$ from the source along its optical axis. To produce the pointlike-source, the light from a white LED is coupled to a 50-μm-diameter pinhole by means of a lens (25.4-mm focal length) and a fiber optic bundle. In this configuration, the diverging light from the pinhole illuminates the mirror and is back reflected to focus onto the pinhole again, in the absence of perturbations in the medium. To get access to the image plane, a beam-splitter cube is placed in front of the pinhole to deviate half of the light reflected from the spherical mirror. To partially block the deviated light and produce the schlieren effect, the razor blade is mounted on a manual translation stage to finely adjust the knife edge at the image point of the source. Light that is deflected by the acoustic wave perturbations in the medium bypassed the blade filter, reaching the camera. In this way, the local variations of the air density are converted into distortions of the collected light, forming the schlieren images. As the light source has a continuous emission mode and the images are obtained with an exposure time of 1 s, what we actually image by schlieren deflectometry is the time-averaged pressure amplitude. In the camera we use an f number of $f/5$, an ISO sensitivity of 800, and a focal length of 248 mm.

B. Results

The experimental results shown in Fig. 5(a) correspond to the normalized pressure amplitude measured along the main axis in the absence of particles (red markers) and the profile extracted from the schlieren image of the acoustic field illustrated in Fig. 5(b) (blue line). There is a one-to-one correspondence between the schlieren profile and the pressure-field amplitude at the central region of the levitator. The red dashed lines in Fig. 5(b) indicate the position of the pressure antinodes. Although particles of different sizes are levitated, Fig. 5(c) exhibits qualitative results for two particles with diameters of $D = 7.02$ mm $= 0.82\lambda$ (top) and 2.30 mm $= 0.27\lambda$ (bottom). In agreement with our theoretical results, the large particle is levitated off axis in the pressure antinode, while the small particle is trapped on axis at the pressure node. An actual photo of three levitated particles is shown in Fig. 5(d), where part of the top and bottom arrays of transducers can be seen as a reference and the inset displays the corresponding schlieren image. As the two cameras captured different perspectives of the same scene, the relative position of the large sphere with respect to the small particles seems shifted from one another, but it is clear that the large

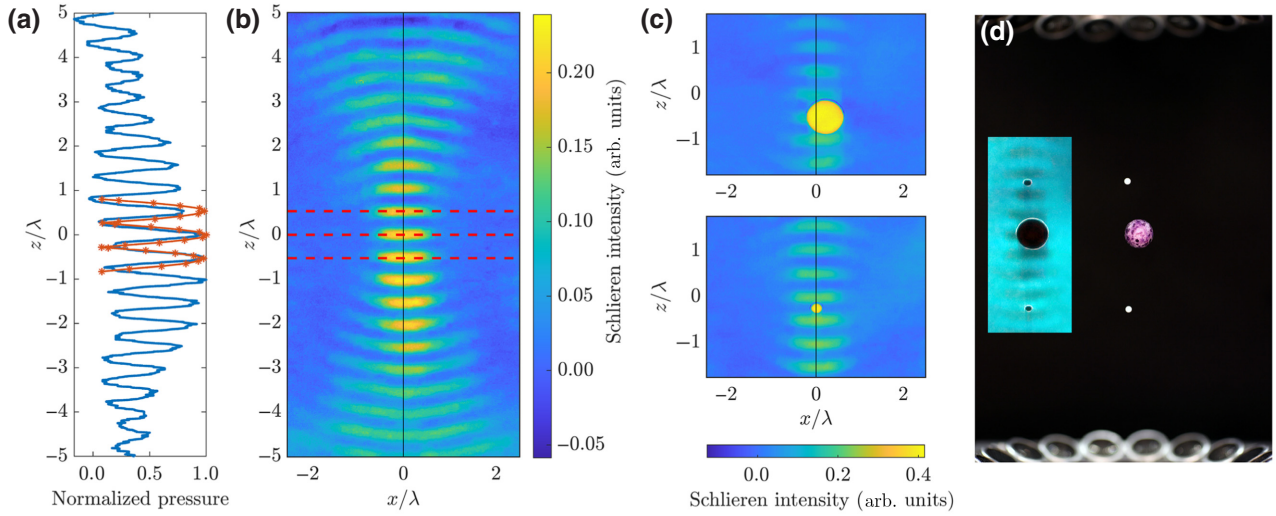

FIG. 5. Experimental results for the acoustic pressure field and the levitation of particles of different sizes. (a) Normalized amplitude of the acoustic pressure measured in the absence of particles (red markers) and the profile along the z axis extracted from the schlieren image of the acoustic field presented in (b) (blue line). The red lines in (b) indicate the location of the antinodes in accordance with the pressure measurements. (c) Processed schlieren images including levitated particles with diameters $D = 7.02$ mm $= 0.82\lambda$ (top) and $D = 2.30$ mm $= 0.27\lambda$ (bottom). (d) Photograph of three particles being simultaneously levitated. The inset shows a raw schlieren image of the same scene from a different perspective.

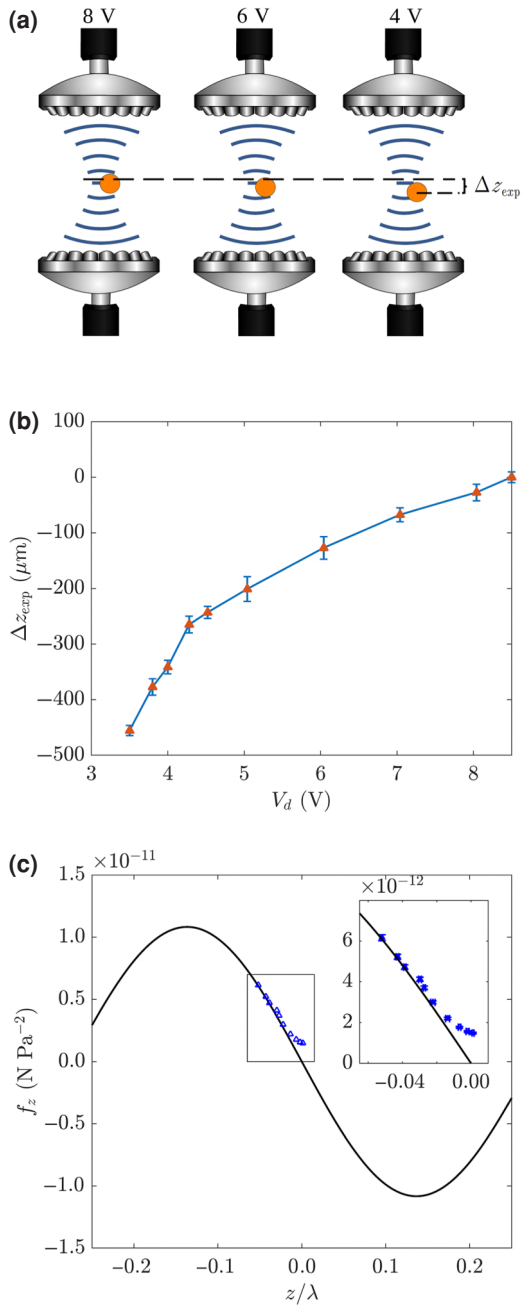

FIG. 6. Quantitative characterization of the axial radiation force. (a) Schematic of the downward displacement of a levitated particle as the driving voltage of the arrays of transducers is decreased (from left to right), reducing the acoustic pressure amplitude. (b) Measured displacement Δz_{exp} of the particle with $D = 0.82\lambda$ as a function of the driving voltage V_d, with respect to the value at $V_d = 8.5$ V. (c) Comparison between the experimental (markers) and the theoretical (solid line) results for the radiation force per Pa^2, $f_z = F_z/P_0^2$ vs z/λ, where $P_0(V_d)$ is the maximum pressure amplitude for a given driving voltage.

particle is off the principal axis of the levitator, which lies along the line joining the two small particles. The colormap of the schlieren pictures is directly correlated with the time-averaged density gradients in the medium due to the acoustic perturbation [35]. In Figs. 5(b) and 5(c) we use false color image processing to enhance contrast; raw schlieren images look as in the inset of Fig. 5(d).

Particles with diameters of approximately 0.67λ are also tested for levitation. However, it is not possible to stably trap them because this particle size approximately corresponds to the transition zone in which sign inversion of the axial force F_z takes place [see Fig. 2(a)]. Videos of three different particles ($D = 0.40\lambda$, 0.67λ, 0.82λ) in the levitator are included in the Supplementary Material [48].

Qualitatively, there is a positive correspondence between the theoretical and experimental results. In addition, we perform a quantitative analysis of the axial radiation force per Pa^2. For this purpose, we characterize the vertical displacement of the equilibrium position (Δz_{exp}) of a levitated sphere as the acoustic pressure level is lowered by reducing the input driving voltage V_d of the arrays of transducers, as schematically illustrated in Fig. 6(a). This experiment is carried out with the sphere of diameter $D = 0.82\lambda$, whose position is analyzed as a function of time using a video-tracking algorithm. The vertical displacement for each voltage, plotted in Fig. 6(b), is determined from the mean position with an associated standard deviation. The maximum driving voltage at the operation frequency (40 kHz) is $V_d = 8.5$ V, which set the reference (zero) value for the displacement measurements. Notice, however, that this point will never correspond to the maximum of the central antinode, $z = 0$, since the particle will always shift downwards by a given distance due to its own weight, regardless of the value of V_d. Indeed, at each equilibrium position, the axial acoustic force F_z balances the weight W of the particle, i.e., $F_z = W$, where $F_z \propto P_0^2(V_d)$ and $P_0(V_d)$ is obtained from the levitator sensitivity [Fig. 4(d)]. Therefore, we can plot the force per Pa^2, $f_z = F_z/P_0^2$, as a function of z, by taking $f_z = W/P_0^2(V_d)$ for each point of the graph 6(b). The experimental results for $f_z(z)$ are depicted with markers in Fig. 6(c), where the corresponding theoretical curve is also plotted (solid black line) for comparison. We note that the measured displacement at the lowest driving voltage (3.5 V), $\Delta z_{\text{exp}} = (-455 \pm 9)$ μm, practically coincide with the calculated value of the equilibrium position for the corresponding pressure amplitude, $P_0(3.5V) = 2.00$ kPa, which gave $z_{\text{eq}} = -452$ μm. This allows us to presume that the shift between the actual position $z = 0$ and the reference we take for the displacement measurement is small enough to lie within the experimental uncertainty and could be neglected. This assumption led to a very good quantitative agreement between the theoretical curve and the experimental results at lower driving voltages [leftmost points in Fig. 6(c)]. Nevertheless, the experimental results for higher driving voltages (rightmost points) depart from the theoretical curve. This is due to a nonlinear dependency between P_0 and V_d arising when the maximum pressure values reach over 3.50 kPa.

IV. CONCLUSIONS AND OUTLOOK

Even though acoustic levitation in midair is nowadays a well-established technique, most of the manipulation strategies so far have relied on the generation and control of the acoustic pressure nodes or low-pressure trapping volumes, assuming that these were the stable equilibrium points for the radiation force. In this work, we demonstrate that there are unnoticed aspects of this physical phenomenon, showing that the size of the particle plays a mayor role to determine its equilibrium positions within a given acoustic field. Through simulations and experiments, we are able to establish that particles with the same density and sizes below approximately 0.6λ have stable equilibrium positions at the pressure nodes of a focused standing wave, whereas particles with sizes between 0.6λ and 1.0λ will be stably trapped nearby the antinodes and off axis, in spite of the rotational symmetry of the field. Furthermore, we demonstrate that particles whose sizes lie within certain ranges are minimally affected by the radiation force, since it is either null all over the space, in the case of a plane standing wave, or very weak, in the case of a focused standing field. This has the largely overlooked implication that levitation devices, operating at a fixed frequency, can fail to levitate particles within specific size ranges.

The size effect can be interpreted in terms of the superposition of multipole partial waves of the field scattered by the particle, which contribute to the total change in the radiation stress tensor [49]. The larger the particle, the more preponderant the role of higher-order multipoles to the scattered field, which interfere among each other and with the incident field, producing a net force pulling the particle either towards the pressure nodes, the antinodes or, in fact, to produce no force at all. Mechanical resonances will arise for particles larger than a wavelength, but the acoustic pressure levels needed to counteract their weight would be growing and nonlinear acoustic effects may appear. The sign inversions of the acoustic force also depend on the characteristics of the levitation device, such as the degree of focusing of the ultrasonic field, which induces additional pressure gradients and determines the curvature of the wave fronts. Indeed, some of the observed effects, like the off-axis trapping position, seem to be curvature driven.

Understanding the size effect is fundamental for acoustic levitation applications. For instance, the shape of the force maps as a function of the size parameter D/λ and the space coordinates remains the same for plane standing waves and it is very similar in the case of focused standing fields for different ultrasonic frequencies, for both axial and transverse force components, implying that our discussion about a maximum force magnitude (highest trapping stiffness) for a given particle size as a fraction of the wavelength has a more general validity. This fact could enhance the performance of the nascent acoustic levitation-based 3D display technology [25,46,50], for example.

Finally, it is worthwhile to point out that the size effect is not a particular feature of the standing-wave levitation trap, although the experimental demonstration becomes very neat by using this configuration. Certainly, any acoustic field with a complex amplitude structure exhibiting alternate regions of higher and lower average pressure could be expected to interact differently with particles, depending on their size and properties. Moreover, this phenomenon is well known in optical traps in the presence of structured light beams and complex optical potentials [51–53]. In that sense, our results pave the way for a deeper understanding of the physical phenomena behind noncontact radiation traps, as well as for the sophistication of acoustic particle manipulation applications.

ACKNOWLEDGMENTS

This work is supported by DGAPA-UNAM, Grants PAPIIT: IN113419, IN109221, and by Universidad del Valle, Grant CI 21182. J. E-M acknowledges CONACYT and PAPIIT-IN113419 for M.Sc. Scholarship. We acknowledge Dr. Santiago Jesús Pérez Ruiz and M.I. Antonio Pérez López from ICAT-UNAM for their valuable assistance in the measurements of pressure against voltage. K.V.-S. and J.L.E. conceived the idea; K.V.-S. coordinated the project; D.B. developed the numerical codes for the calculation of acoustical forces; J.F.P.O. and J.E.-M. adapted the codes and made the numerical analysis; V.C. designed and conducted the levitation experiments, including the schlieren visualization and relative pressure measurements *in situ*; J.F.P.O., J.L.E., and V.C. characterized the acoustic pressure field and its dependency on the levitator driving voltage; K.V.-S. wrote the first version of the paper; all the authors contributed to the development of the research, the discussion, and the edition of the paper.

[1] A. Kundt, Ueber eine neue art akustischer staubfiguren und über die anwendung derselben zur bestimmung der schallgeschwindigkeit in festen körpern und gasen, Ann. Phys. **203**, 497 (1866).
[2] J. L. R. Strut, *Theory of Sound, Volume II* (Cambridge Library Collection - Physical Sciences. Cambridge University Press, Cambridge, England, 2001).
[3] L. V. King, On the acoustic radiation pressure on spheres, Proc. R. Soc. London. Ser. A-Math. Phys. Sci. **147**, 212 (1934).
[4] L. P. Gor'kov, On the forces acting on a small particle in an acoustical field in an ideal fluid, Doklady Akademii Nauk SSSR. **140**, 88 (1961).
[5] M. A. Andrade, N. Pérez, and J. C. Adamowski, Review of progress in acoustic levitation, Braz. J. Phys. **48**, 190 (2018).
[6] E. Brandt, Suspended by sound, Nature **413**, 474 (2001).
[7] H. Bruus, Acoustofluidics 7: The acoustic radiation force on small particles, Lab Chip **12**, 1014 (2012).

[8] K. Bücks and H. Müller, Über einige beobachtungen an schwingenden piezoquarzen und ihrem schallfeld, Z. Phys. **84**, 75 (1933).

[9] R. Whymark, Acoustic field positioning for containerless processing, Ultrasonics **13**, 251 (1975).

[10] E. Trinh, Compact acoustic levitation device for studies in fluid dynamics and material science in the laboratory and microgravity, Rev. Sci. Instrum. **56**, 2059 (1985).

[11] A. Yarin, G. Brenn, O. Kastner, D. Rensink, and C. Tropea, Evaporation of acoustically levitated droplets, J. Fluid. Mech. **399**, 151 (1999).

[12] S. Santesson and S. Nilsson, Airborne chemistry: Acoustic levitation in chemical analysis, Anal. Bioanal. Chem. **378**, 1704 (2004).

[13] F. Priego-Capote and L. de Castro, Ultrasound-assisted levitation: Lab-on-a-drop, TrAC Trends Anal. Chem. **25**, 856 (2006).

[14] D. Zang, Y. Yu, Z. Chen, X. Li, H. Wu, and X. Geng, Acoustic levitation of liquid drops: Dynamics, manipulation and phase transitions, Adv. Colloid Interface Sci. **243**, 77 (2017).

[15] V. Contreras, R. Valencia, J. Peralta, H. Sobral, M. Meneses-Nava, and H. Martinez, Chemical elemental analysis of single acoustic-levitated water droplets by laser-induced breakdown spectroscopy, Opt. Lett. **43**, 2260 (2018).

[16] B. R. Wood, P. Heraud, S. Stojkovic, D. Morrison, J. Beardall, and D. McNaughton, A portable raman acoustic levitation spectroscopic system for the identification and environmental monitoring of algal cells, Anal. Chem. **77**, 4955 (2005).

[17] Y. A. Tobon, S. Seng, L. A. Picone, Y. B. Bava, L. C. Juncal, M. Moreau, R. M. Romano, J. Barbillat, and S. Sobanska, Photochemistry of single particles using acoustic levitation coupled with raman microspectrometry, J. Raman Spectrosc. **48**, 1135 (2017).

[18] H. Grosshans, M. Griesing, M. Mönckedieck, T. Hellwig, B. Walther, S. R. Gopireddy, R. Sedelmayer, W. Pauer, H.-U. Moritz, N. A. Urbanetz, and Eva Gutheil, Numerical and experimental study of the drying of bi-component droplets under various drying conditions, Int. J. Heat Mass Transf. **96**, 97 (2016).

[19] A. Marzo, in *Acoustic Levitation* (Springer, Singapore, 2020), p. 11.

[20] W. Xie and B. Wei, Parametric study of single-axis acoustic levitation, Appl. Phys. Lett. **79**, 881 (2001).

[21] W. J. Xie, C. D. Cao, Y. J. Lü, and B. Wei, Levitation of Iridium and Liquid Mercury by Ultrasound, Phys. Rev. Lett. **89**, 104304 (2002).

[22] D. Foresti, M. Nabavi, M. Klingauf, A. Ferrari, and D. Poulikakos, Acoustophoretic contactless transport and handling of matter in air, Proc. Natl. Acad. Sci. **110**, 12549 (2013).

[23] S. Bauerecker and B. Neidhart, Formation and growth of ice particles in stationary ultrasonic fields, J. Chem. Phys. **109**, 3709 (1998).

[24] Y. Ochiai, T. Hoshi, and J. Rekimoto, Three-dimensional mid-air acoustic manipulation by ultrasonic phased arrays, PLoS ONE **9**, e97590 (2014).

[25] Y. Ochiai, T. Hoshi, and J. Rekimoto, Pixie dust: Graphics generated by levitated and animated objects in computational acoustic-potential field, ACM Trans. Graphics (TOG) **33**, 1 (2014).

[26] A. Marzo, S. A. Seah, B. W. Drinkwater, D. R. Sahoo, B. Long, and S. Subramanian, Holographic acoustic elements for manipulation of levitated objects, Nat. Commun. **6**, 8661 (2015).

[27] A. Marzo, A. Barnes, and B. W. Drinkwater, TinyLev: A multi-emitter single-axis acoustic levitator, Rev. Sci. Instrum. **88**, 085105 (2017).

[28] A. Ashkin and J. M. Dziedzic, Observation of Resonances in the Radiation Pressure on Dielectric Spheres, Phys. Rev. Lett. **38**, 1351 (1977).

[29] S. Ueha, Y. Hashimoto, and Y. Koike, Non-contact transportation using near-field acoustic levitation, Ultrasonics **38**, 26 (2000).

[30] S. Zhao and J. Wallaschek, A standing wave acoustic levitation system for large planar objects, Arch. Appl. Mech. **81**, 123 (2011).

[31] M. A. Andrade, A. L. Bernassau, and J. C. Adamowski, Acoustic levitation of a large solid sphere, Appl. Phys. Lett. **109**, 044101 (2016).

[32] A. Marzo, M. Caleap, and B. W. Drinkwater, Acoustic Virtual Vortices with Tunable Orbital Angular Momentum for Trapping of Mie Particles, Phys. Rev. Lett. **120**, 044301 (2018).

[33] S. Inoue, S. Mogami, T. Ichiyama, A. Noda, Y. Makino, and H. Shinoda, Acoustical boundary hologram for macroscopic rigid-body levitation, J. Acoust. Soc. Am. **145**, 328 (2019).

[34] D. Baresch, J.-L. Thomas, and R. Marchiano, Three-dimensional acoustic radiation force on an arbitrarily located elastic sphere, J. Acoust. Soc. Am. **133**, 25 (2013).

[35] V. Contreras and A. Marzo, Adjusting single-axis acoustic levitators in real time using rainbow schlieren deflectometry, Rev. Sci. Instrum. **92**, 015107 (2021).

[36] B. Maheu, G. Gouesbet, and G. Gréhan, A concise presentation of the generalized lorenz-mie theory for arbitrary location of the scatterer in an arbitrary incident profile, J. Opt. **19**, 59 (1988).

[37] G. T. Silva, An expression for the radiation force exerted by an acoustic beam with arbitrary wavefront (l), J. Acoust. Soc. Am. **130**, 3541 (2011).

[38] D. Baresch, J.-L. Thomas, and R. Marchiano, Spherical vortex beams of high radial degree for enhanced single-beam tweezers, J. Appl. Phys. **113**, 184901 (2013).

[39] M. A. S. Pessôa and A. A. R. Neves, Acoustic scattering and forces on an arbitrarily sized fluid sphere by a general acoustic field, J. Sound. Vib. **479**, 115373 (2020).

[40] D. Baresch, J.-L. Thomas, and R. Marchiano, Observation of a Single-Beam Gradient Force Acoustical Trap for Elastic Particles: Acoustical Tweezers, Phys. Rev. Lett. **116**, 024301 (2016).

[41] D. Baresch and V. Garbin, Acoustic trapping of microbubbles in complex environments and controlled payload release, PNAS **117**, 15490 (2020).

[42] R. Habibi, C. Devendran, and A. Neild, Trapping and patterning of large particles and cells in a 1D ultrasonic standing wave, Lab Chip **17**, 3279 (2017).

[43] L. Brillouin, *Tensors in Mechanics and Elasticity* (Academic Press, New York, 1964).

[44] T. Hasegawa and K. Yosioka, Acoustic radiation force on fused silica spheres, and intensity determination, J. Acoust. Soc. Am. **58**, 581 (1975).

[45] P. L. Marston, Axial radiation force of a bessel beam on a sphere and direction reversal of the force, J. Acoust. Soc. Am. **120**, 3518 (2006).

[46] R. Hirayama, D. M. Plasencia, N. Masuda, and S. Subramanian, A volumetric display for visual, tactile and audio presentation using acoustic trapping, Nature **575**, 320 (2019).

[47] G. S. Settles, *Schlieren and Shadowgraph Techniques: Visualizing Phenomena in Transparent Media* (Springer Science & Business Media, Berlin, Germany, 2001).

[48] See Supplemental Material at http://link.aps.org/supplemental/10.1103/PhysRevApplied.18.034026 for videos of three different particles in the acoustic levitation device: $D = 0.82\lambda$ (left), trapped at an antinode; $D = 0.67\lambda$ (center), which could not be trapped; $D = 0.40\lambda$ (right), trapped at a node.

[49] J.-L. Thomas, R. Marchiano, and D. Baresch, Acoustical and optical radiation pressure and the development of single beam acoustical tweezers, J. Quant. Spectrosc. Radiat. Transfer **195**, 55 (2017).

[50] T. Fushimi, A. Marzo, B. W. Drinkwater, and T. L. Hill, Acoustophoretic volumetric displays using a fast-moving levitated particle, Appl. Phys. Lett. **115**, 064101 (2019).

[51] P. Zemánek, A. Jonáš, L. Šrámek, and M. Liška, Optical trapping of nanoparticles and microparticles by a Gaussian standing wave, Opt. Lett. **24**, 1448 (1999).

[52] I. Ricárdez-Vargas, P. Rodríguez-Montero, R. Ramos-García, and K. Volke-Sepúlveda, Modulated optical sieve for sorting of polydisperse microparticles, Appl. Phys. Lett. **88**, 121116 (2006).

[53] G. Milne, K. Dholakia, D. McGloin, K. Volke-Sepulveda, and P. Zemánek, Transverse particle dynamics in a Bessel beam, Opt. Express **15**, 13972 (2007).